










SN 2021wvw: A Core-collapse Supernova at the Subluminous, Slower, and Shorter End of Type IIPs

Rishabh Singh Teja^{1,2} , Jared A. Goldberg³ , D. K. Sahu¹ , G. C. Anupama¹ , Avinash Singh^{4,5} , Vishwajeet Swain⁶ , and Varun Bhalerao⁶ 

¹ Indian Institute of Astrophysics, II Block, Koramangala, Bengaluru-560034, Karnataka, India; rishabh.teja@iiap.res.in, rsteja001@gmail.com

² Pondicherry University, R.V. Nagar, Kalapet, Pondicherry-605014, UT of Puducherry, India

³ Center for Computational Astrophysics, Flatiron Institute, 162 5th Avenue, New York, NY 10010, USA

⁴ Oskar Klein Centre, Department of Astronomy, Stockholm University, Albanova University Centre, SE-106 91 Stockholm, Sweden

⁵ Hiroshima Astrophysical Science Center, Hiroshima University, Higashi-Hiroshima, Hiroshima 739-8526, Japan

⁶ Department of Physics, Indian Institute of Technology Bombay, Powai, Mumbai 400076, India

Received 2024 June 11; revised 2024 July 9; accepted 2024 July 17; published 2024 October 3

Abstract

We present detailed multiband photometric and spectroscopic observations and analysis of a rare core-collapse supernova, SN 2021wvw, that includes photometric evolution up to 250 days and spectroscopic coverage up to 100 days postexplosion. A unique event that does not fit well within the general trends observed for Type IIP supernovae, SN 2021wvw shows an intermediate luminosity with a short plateau phase of just about 75 days, followed by a very sharp (~ 10 days) transition to the tail phase. Even in the velocity space, it lies at a lower velocity compared to a larger Type II sample. The observed peak absolute magnitude is -16.1 mag in r -band, and the nickel mass is well constrained to $0.020 \pm 0.006 M_{\odot}$. Detailed hydrodynamical modeling using MESA +STELLA suggests a radially compact, low-metallicity, high-mass red supergiant progenitor ($M_{\text{ZAMS}} = 18 M_{\odot}$), which exploded with $\sim 0.2 \times 10^{51}$ erg s^{-1} leaving an ejecta mass of $M_{\text{ej}} \approx 5 M_{\odot}$. Significant late-time fallback during the shock propagation phase is also seen in progenitor+explosion models consistent with the light-curve properties. As the faintest short-plateau supernova characterized to date, this event adds to the growing diversity of transitional events between the canonical ~ 100 days plateau Type IIP and stripped-envelope events.

Unified Astronomy Thesaurus concepts: Core-collapse supernovae (304); Type II supernovae (1731); Red supergiant stars (1375); Observational astronomy (1145)

Materials only available in the online version of record: data behind figure, machine-readable table

1. Introduction

Stars with mass $\gtrsim 8 M_{\odot}$ end their lives as energetic cosmic explosions called core-collapse supernovae (CCSNe). Depending on factors such as the initial mass, rotation, evolutionary track, retained envelope, immediate surroundings, and explosion energy, their light curves come in various shapes and brightness, and there are differences in their spectral features as well. Persistent hydrogen features in the spectra indicate a Type II class SN; otherwise, a Type I SN (Filippenko 1997). There is a further distinction in the light-curve evolution of the Type IIs, with either a linear decline (Type IIL) or with a slow, plateau-like decline (Type IIP) followed by a linear decline (Barbon et al. 1979). Although appearing distinct, it is becoming increasingly evident that there is no clear boundary between the IIP and IIL subclasses, and these are merely a continuous sequence of the Type II class (Anderson et al. 2014; Pessi et al. 2019).

Within the Type IIP subclass, there appears to be a certain amount of inhomogeneity concerning the plateau length. In most cases, the plateau length is, on an average, 100 days. However, recent observations have shown several events that deviate from this 100 days plateau length on either side, from the shorter end of the plateau ($\sim 4\%$, Eldridge et al. 2018; Hiramatsu et al. 2021) to the long plateau phase ($\sim 0.35\%$ for > 140 days,

Eldridge et al. 2018). A few examples of the short-plateau SNe are SN 2006Y (55 days), SN 2006ai (60 days) (Hiramatsu et al. 2021), SN 2020jfo (65 days) (Sollerman et al. 2021; Teja et al. 2022), and SN 2018gj (70 days) (Teja et al. 2023a), while SN 2005cs (110 days) (Tsvetkov et al. 2006; Pastorello et al. 2009), SN 2018hwm (130 days) (Reguitti et al. 2021), and SN 2020cxd (120 days) and SN 2021aai (140 days) (Valerin et al. 2022) had a longer plateau duration. In addition, there is also a very heterogeneous distribution in the brightness space for this subclass (Valenti et al. 2016). With more discoveries and extensive follow-up in recent times, many events are found to be intrinsically fainter compared to typical Type II SNe (mean $M_{V\text{max}} \sim -16.7$, Anderson et al. 2014) and are termed as low ($M_V \geq -15$ mag) or intermediate ($M_V \approx -16$ mag) luminosity SNe. These low/intermediate-luminosity SNe also predominantly show a plateau length of 100 days or more (for instance ≥ 140 days in SN 2016bkv, Nakaoka et al. 2018; Valerin et al. 2022; Fang et al. 2024). Current understanding attributes these SNe to originate from weak explosions of the lower mass end of the red supergiant (RSG) stars, typically less than $15 M_{\odot}$ with low ^{56}Ni mass production (Pumo et al. 2017; Lisakov et al. 2018).

On the other hand, several short-plateau SNe (50–80 days) studies show these to be brighter than the typical Type IIP SNe (Hiramatsu et al. 2021; Teja et al. 2022), with the low-luminosity, short-plateau events being infrequent. Type II SNe with short plateau also tend to decline faster during their plateau phase (Hiramatsu et al. 2021). The favored mechanism for these short-plateau SNe is still debated. A common trend is that

the light-curve properties require a small but nonnegligible H-rich envelope (\approx a few M_{\odot}) at the time of explosion (Hiramatsu et al. 2021). Single-star evolutionary scenarios tend to favor moderate to high initial mass RSGs because stronger winds in more massive progenitors provide a channel for stars to lose the majority but not the entirety of their H-rich envelope (see, e.g., Dessart et al. 2010; Sukhbold et al. 2016; Curtis et al. 2021). Other theoretical works remain agnostic to the mass-loss mechanism or directly link low envelope mass with binary interaction (e.g., Morozova et al. 2015; Paxton et al. 2018; Dessart et al. 2024), and a growing body of observational works investigate potential low-mass RSG origins as well (Teja et al. 2022, 2023a; Utrobin & Chugai 2024), with one being a direct detection (Sollerman et al. 2021). In both progenitor-mass regimes, the envelope mass lost by the progenitor is high.

The occurrence of the short-plateau events is relatively low. While the low luminosity ones might suffer from an observational bias, this cannot be said about most short-plateau events because they are usually bright. Even taking binarity into account, population-focused studies (e.g., Eldridge et al. 2018; Ercolino et al. 2024) nonetheless indicate their rates are expected to be low (\sim 4%).

This work presents comprehensive optical spectroscopic and photometric observations of SN 2021wvw, a distinctive short-plateau Type IIP supernova. SN 2021wvw (other names: PS21jnb, ZTF21abvxcxl, ATLAS21bgtz, Gaia21eqm) was discovered on 2021 August 24, 14:32.6UT (JD = 2459451.1) in UGC 02605 (Jones et al. 2021) with 17.93 ABMag in the $i - P1$ filter. Subsequently, it was classified as Type II with a strong blue continuum having P-Cygni $H\alpha$ and $H\beta$ emissions (Hinkle 2021). The first detection in ZTF- g filter (19.34 mag) was on JD 2459449.95 and the last nondetection in ZTF- r filter (19.15 mag) was on JD 2459449.91. Using this, we obtain JD 2459449.93 ± 0.02 as the explosion epoch. A similar epoch, shifted by +0.2 days, is obtained using data from ATLAS forced photometry server with 5σ last nondetection (>18.89 mag) on JD 2459449.1 and first detection (18.10 ± 0.08 mag) on JD 2459451.1 both in ATLAS- o filter. The nondetections in both ZTF- r and ATLAS- o are at a similar epoch, hence we consider this as the last nondetection and the first detection in ZTF g -band. Using this, we obtain $t_{\text{exp}} = 2459449.9 \pm 0.3$ as the explosion epoch and use this throughout. The location of SN 2021wvw in its host galaxy is marked in Figure 1.

The structure of this paper is as follows: Section 2 provides details of various data sources utilized. The light curves and spectra are analyzed and compared in Sections 3 and 4, respectively, along with estimating ^{56}Ni mass and expansion velocities. Section 5 explores the probable progenitor using various models, including complete hydrodynamical modeling, followed by a general discussion in Section 6. We summarize this work in Section 7.

2. Photometry and Spectroscopy: Data Sources

We began photometry of SN 2021wvw in the optical +8.4 days past explosion using the 0.7 m robotic GROWTH-India Telescope (GIT; Kumar et al. 2022) and the 2.0 m Himalayan Chandra Telescope (HCT), both situated at the Indian Astronomical Observatory (IAO; Prabhu 2014), Hanle, India. GIT covered dense multiband photometry in SDSS- $g'r'i'z'$ filters, and HCT covered photometry in Bessell- V and $-R$ filters. We supplemented our observations with photometry

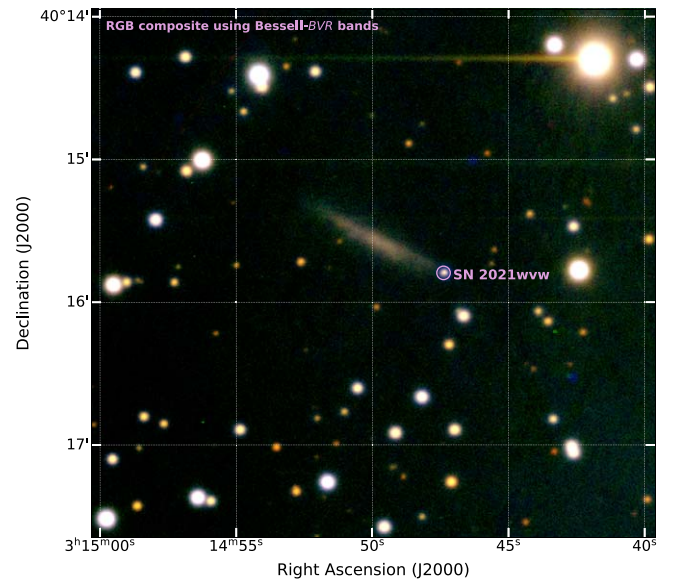


Figure 1. RGB color composite finder chart for SN2021wvw utilizing Bessell- BVR filters from HCT.

from the Asteroid Terrestrial-impact Last Alert System (ATLAS; Tonry et al. 2018; Smith et al. 2020) forced photometry server (Shingles et al. 2021) in c and o filters. We also obtained ZTF (Bellm et al. 2019) $-g$ and $-r$ filter apparent magnitudes from ALerCE (Förster et al. 2021). The ATLAS photometry, being noisy, has been binned for 2 day intervals in the late phase using Young (2020) python script. During the late phase, we took multiple exposures using GIT and HCT and summed them for a better signal-to-noise ratio in respective filters. Since the SN is far away from the host nucleus ($\sim 31''$) and at the periphery, we do not perform any template subtraction. The last detected photometric points are significantly brighter (1.5–3 mag) than the SDSS photometry⁷ in the regions around the host center and near the SN position. Standard photometric data reduction procedures have been adopted utilizing IRAF and pyraf, the details of which can be found in Teja et al. (2023a). The photometric data are tabulated in the Appendix of this work.

We obtained low-resolution ($R \sim 800$) optical spectra with the HFOSC instrument available on HCT using 167 l slit ($1''92$ width and $11'$ length). The spectra observed with grisms Gr7 and Gr8 were combined to obtain spectra covering a wavelength range of 4000–9000 Å (spectra logs are in Table 1). The optical spectra were obtained during 5–95 days postexplosion. Beyond 95 days, the SN faded considerably, and spectroscopy with HCT was not feasible. The observed 2D spectra were bias corrected using nightly bias frames, and the 1D spectra were optimally extracted. The wavelength correction was performed using the dispersion solutions obtained from several arc lamps (FeNe, FeAr) spectra. The night-sky emission lines (5577, 6300, 6363 Å) in the background spectra were used to perform the accurate wavelength calibrations, applying small shifts wherever required. Spectrophotometric standards were observed periodically to correct the instrumental response and finalize the spectra in the flux scale. Eventually, a single flux-calibrated spectrum was obtained after combining spectra from

⁷ <https://skyserver.sdss.org/dr18/>

Table 1

Log of Spectroscopic Observations of SN 2021wvw Obtained from HCT

Date (yyyy-mm-dd)	JD (2459000+)	Phase ^a (days)	Range (Å)
2021-08-28	455.4	5.5	4000–7700
2021-09-13	471.3	21.4	4000–8900
2021-09-18	476.3	26.3	4000–8900
2021-09-19	477.4	27.4	4000–7700
2021-09-29	487.3	37.3	4000–8900
2021-10-02	490.2	40.3	4000–8900
2021-10-09	497.2	47.3	4000–8900
2021-10-10	498.2	48.3	4000–8900
2021-10-14	502.2	52.2	4000–8900
2021-10-19	507.2	57.3	4000–8900
2021-10-21	509.1	59.2	4000–8900
2021-10-22	510.2	60.3	5300–8900
2021-10-26	514.2	64.2	4000–8900
2021-10-30	518.2	68.3	4000–8900
2021-11-08	527.1	77.2	4000–8900
2021-11-15	534.3	84.4	4000–8900
2021-11-26	545.1	95.1	4000–7700

Note.^a Phase given for $t_{\text{exp}} = 2459449.9$ JD.

individual grisms. All these steps were performed using various tasks in IRAF.

The host redshift ($z = 0.0099$, Schneider et al. 1992) and line-of-sight extinction ($E(B - V) = 0.24$ mag, Schlafly & Finkbeiner (2011)) are taken from the NASA/IPAC Extragalactic Database and IRSA, respectively. The redshift corresponds to a distance of 41.51 ± 2.91 Mpc or $\mu = 33.09 \pm 0.15$ mag, assuming the Λ CDM cosmology with $H_0 = 72.5 \text{ km s}^{-1} \text{ Mpc}^{-1}$ (Riess et al. 2022). We used Cardelli et al. (1989) extinction law with $R_V = 3.1$ to correct for Galactic reddening. We do not find any discernible DNaI features at redshift of the host galaxy in SN spectra, and hence assume no extinction due to the host galaxy.

3. Light-curve Evolution

We present the panchromatic light-curve evolution of SN 2021wvw in Figure 2. The light-curve evolution spans roughly 220 days postexplosion. Other than the bluer bands such as g -band, the light curves evolution in different filters show a very flat evolution up to 70–80 days before transitioning sharply into the tail phase. The plateau and transition phases are very densely sampled in most filters. In R and V filters, the tail phase is sampled up to 220 days. We estimate a plateau length of around 75 days (OPTd, Anderson et al. 2014) and a sharp transition period of about 10 days.

The midplateau absolute magnitude is $\approx -16.0 \pm 0.1$ mag in r -band. It puts SN 2021wvw in the intermediate-luminosity regime for Type IIP SNe. The duration of the plateau phase is also shorter (~ 75 days), whereas the typical plateau lengths for Type IIP SNe are ~ 100 days and even longer in the case of underluminous SNe (SN 2005cs, SN 2016bkv, SN 2021gmj). In Figure 3, the SN 2021wvw r -band light curve is compared with r/R -band light curves of other intermediate/low-luminosity and short-plateau SNe, respectively. We compare with the archetypal SN 2005cs (Pastorello et al. 2006) and SN 2021gmj (Murai et al. 2024) for low-luminosity SNe. Although short plateaus are very rare in the overall Type II SNe, we compare

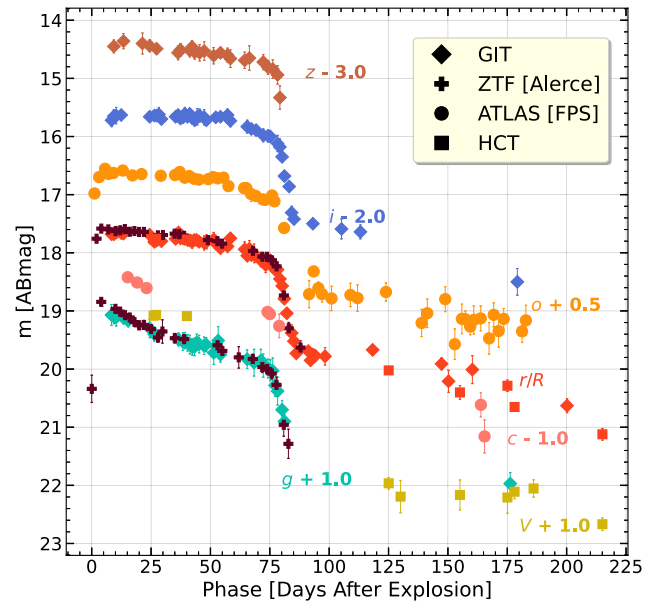


Figure 2. Light-curve evolution of SN 2021wvw for various filters from GIT and HCT is shown. The light curves also include data from ZTF and ATLAS surveys. The constants added to the individual light curves are for visual clarity.

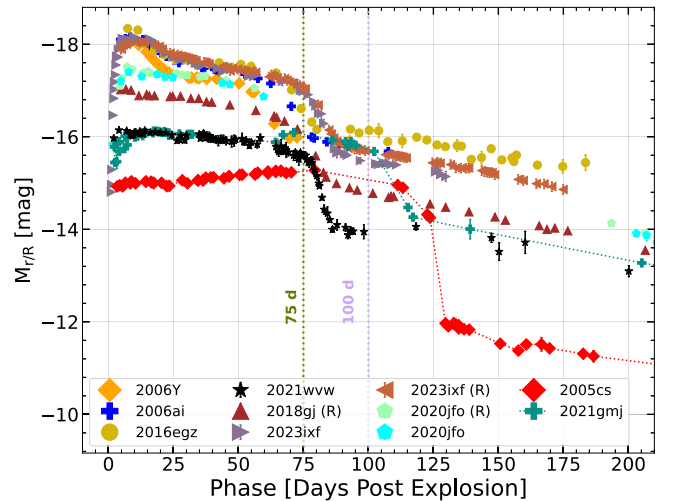


Figure 3. SN 2021wvw r -band light-curve evolution is compared with the r/R -band light curves of other short-plateau SNe. We also show the archetypal low-luminosity SN 2005cs and an intermediate-luminosity SN 2021gmj.

with other well-studied short-plateau SNe in the literature, such as SN 2006Y, SN 2006ai, SN 2016egz (Hiramatsu et al. 2021), SN 2018gj (Teja et al. 2023a), SN 2020jfo (Teja et al. 2022), and SN 2023ixf (Teja et al. 2023b; Singh et al. 2024).

The photospheric phase light-curve evolution of SN 2021wvw, particularly for r - and i -bands, is gradual, which is atypical for short-plateau SNe, for which the decline is generally rapid (Hiramatsu et al. 2021). Although the early (s_1) phase after maximum is not evident in the multiband light curves, upon closer inspection the g - and r -bands show a gradual decline in the postpeak evolution. We find this to be $2.52^{+0.52}_{-0.53} \text{ mag } 100 \text{ day}^{-1}$ and $0.34^{+0.19}_{-0.19} \text{ mag } 100 \text{ day}^{-1}$ in g - and r -band, respectively, whereas the decline is much steeper in other objects; for example, SN 2006Y and SN 2006ai have $4.62^{+0.51}_{-0.52} \text{ mag } 100 \text{ day}^{-1}$ and $4.44^{+0.05}_{-0.05} \text{ mag } 100 \text{ day}^{-1}$, respectively, in g -band. We also estimated the decline rates of the

Table 2
Various Slopes Obtained for Different Phases of Light Curves are Presented

SN	g [mag (100 day) $^{-1}$]		r/R [mag (100 day) $^{-1}$]			i [mag (100 day) $^{-1}$]		$M_{r/R}$ (mag)
	s1	s2	s1	s2	s3	s2	s3	
2021wvw	2.52 ± 0.53	1.25 ± 0.16	0.34 ± 0.19	0.78 ± 0.17	0.64 ± 0.28	0.10 ± 0.13	1.09 ± 0.25	-16.0
2005cs	-0.53 ± 0.01	0.60 ± 0.02	-15.2
2006Y	4.62 ± 0.51	3.28 ± 0.10	4.75 ± 0.13	0.29 ± 0.20	...	1.22 ± 0.10	...	-17.3
2006ai	4.44 ± 0.05	2.86 ± 0.06	4.01 ± 0.10	0.96 ± 0.04	1.03 ± 0.13	1.01 ± 0.04	1.53 ± 0.19	-17.5
2016egz	...	2.83 ± 0.19	...	0.89 ± 0.13	1.11 ± 0.04	1.51 ± 0.17	1.10 ± 0.10	-17.6
2021gmj	0.25 ± 0.01	0.51 ± 0.11	1.28 ± 0.02	1.27 ± 0.03	-15.9

Note. Slopes and absolute magnitude for other SNe are also compared. The absolute magnitudes ($M_{r/R}$) are reported from the middle of the plateau.

plateau phase (s2) and tail phase (s3). The estimated values of various slopes and the midplateau absolute magnitudes are shown in Table 2. Interestingly, the plateau phase in the i -band for SN 2021wvw is almost nondeclining with $s2 = 0.10 \pm 0.13$ mag 100 day $^{-1}$, whereas for other SNe, both with lower luminosity and shorter-plateau SNe, it is around an order of magnitude higher. Evidently, the tail phase decline ($s3 = 0.64 \pm 0.28$ mag 100 day $^{-1}$) of SN 2021wvw in the r -band is close to the values obtained for other lower luminosity SNe (SN 2021gmj, SN 2005cs). At a similar phase, slope s3 in the i -band is nondifferentiable for both low-luminosity and short-plateau SNe with values ranging from 1.1 to 1.5 mag 100 day $^{-1}$.

Comparing the midplateau luminosity ($M_{\text{tp}1/2}$) in r/R -band with other SNe, we find that SN 2021wvw has a similar magnitude as of SN 2021gmj (-15.9 mag), and about 1 mag higher than the $M_{\text{tp}1/2}$ of SN 2005cs (-15.2 mag). $M_{\text{tp}1/2}$ of a majority of other short-plateau SNe is higher than -17 mag except for SN 2018gj (-16.7 mag) as shown in Figure 3.

3.1. Radioactive ^{56}Ni

The late-time evolution is primarily powered by the radioactive decay of ^{56}Ni formed during explosive nucleosynthesis. It is the ultimate powering source in the Type II SNe during the nebular phase. Hence, the late-time bolometric light curve can provide tight constraints on estimating the ^{56}Ni mass. We use SuperBol (Nicholl 2018) to estimate the pseudobolometric light curve and a complete bolometric light curve evolution from extrapolated blackbody estimates. The extinction-corrected multiband light curves were used as input, taking well-sampled r -band as the reference light curve. The filters utilized for the pseudobolometric curves were *groiz*.

We estimate the ^{56}Ni using the following equation given in Yuan et al. (2016), which also takes into account the γ -ray leakage in case of a stripped envelope:

$$L_{\text{obs}}(t) = L_0 \times M_{\text{Ni}} \times \left[e^{-\left(\frac{\Delta t}{t_{\text{Co}}}\right)} - e^{-\left(\frac{\Delta t}{t_{\text{Ni}}}\right)} \right] \times \left(1 - e^{-\left(\frac{t_c^2}{(\Delta t)^2}\right)} \right)$$

where, $\Delta t = t - t_{\text{exp}}$, L_0 , t_{Co} , and t_{Ni} are 1.41×10^{43} erg s $^{-1}$, 111.4 and 8.8 days, respectively. Here, t_c is the characteristic time when the optical depth for γ -rays approaches unity (Yuan et al. 2016). We use *scipy* and *emcee* packages to fit and estimate errors in the values. Using the pseudobolometric light curve, we estimate ^{56}Ni mass as $0.011 \pm 0.001 M_{\odot}$. This provides a lower limit on the ^{56}Ni mass. In addition, considering the blackbody fitted luminosity as bolometric luminosity, we obtain $M_{^{56}\text{Ni}} = 0.023 \pm 0.003 M_{\odot}$, which we consider as an upper limit for the estimated values. The latter value is more

than twice what was obtained using the pseudobolometric light curve, but, synonymous with a $\sim 50\%$ NIR contribution seen in the nebular phase of SN 2023ixf (Singh et al. 2024). We lack NIR data to provide more information about the accuracy of the contribution in the late phase. Nevertheless, the ^{56}Ni mass estimated implies a significant NIR flux contribution at late phases. Hence, NIR observations for such objects in the nebular phase are crucial for a better understanding. In subsequent sections, we perform light-curve modeling to constrain the nickel mass and other parameters more robustly.

4. Spectra

We present a complete spectral evolution of SN 2021wvw covering the plateau and transition phases in Figure 4. The spectra have been calibrated with the corresponding multiband fluxes, corrected for the host redshift, and dereddened with the estimated extinction. The phases mentioned are with respect to the estimated explosion epoch. All the well-identified lines are marked for clarity in the figure.

4.1. Evolution and Comparisons

The first spectrum was obtained at +5.5 days. The spectrum comprises a blue continuum with broad Balmer features and He I $\lambda 5876$ superposed on it. After that, there is a gap of around 15 days; the following spectrum is on +21 days. Thereafter, the spectral evolution is densely sampled until the supernova enters the nebular phase. Qualitatively, absorption features appear relatively narrow at first glance compared to typical IIP SNe, indicating relatively low velocities, and they become narrower with time. Although there are some hints of Fe II in the bluer region at +21 days, these features do not evolve much until +37 days, after which we start to see Fe II lines conspicuously. Around +21 days, we also observe the appearance of Ca NIR triplet feature in the redward region, strengthening as the SN ejecta evolves further in the photospheric phase. Interestingly, the region between Fe II lines and H α is devoid of any lines except a weak appearance of DNa I from +37 days onward. Similarly, the region between H α and Ca triplet lacks any discernible features until the end of the observed evolution. We observe a band of emission lines between H β and H γ , usually attributed to Fe lines.

The midplateau and end-plateau spectra are modeled using SYNAPPS/Syn++ (Thomas et al. 2011) to better ascertain the minimum number of species required to explain the observed spectra. SYNAPPS/Syn++ is a direct implementation of parameterized spectral synthesis code SYNOW (Parrent et al. 2010). It assumes a spherical symmetry with homologous expansion of the ejecta. The emission of photons is from a

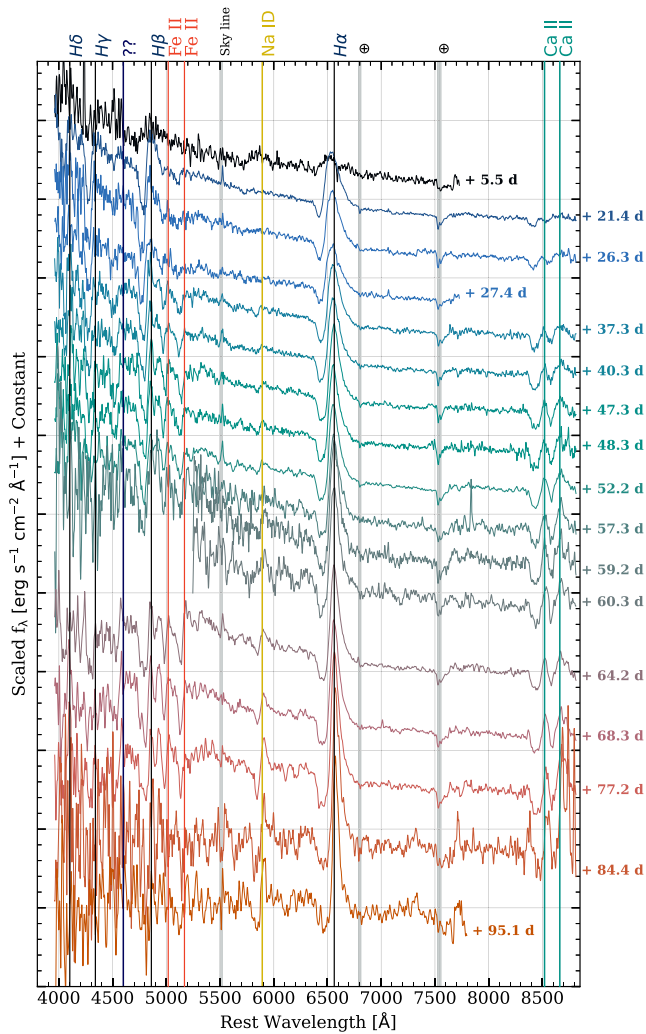


Figure 4. Spectral sequence for SN 2021wvw. The spectra have been corrected for absolute flux using corresponding photometry and also dereddened using MW LOS extinction.

(The data used to create this figure are available in the [online article](#).)

sharp photosphere, with the optical depth taken as an exponential function of velocity,

$$\tau_{\text{ref}}(v) = \tau_{\text{ref}}(v_{\text{ref}}) \exp\left(\frac{v_{\text{ref}} - v}{v_e}\right),$$

where v_{ref} is reference velocity for parameterization and v_e is the maximum velocity allowed at the outer edge of the line-forming region (Thomas et al. 2011). For a particular optical depth, the reference line profile is estimated for a given ion with the remaining lines following Boltzmann statistics (Parrent et al. 2010). SYNAPPS iteratively generates synthetic spectra based on a provided input file with parameters such as ions list, blackbody temperature, expansion velocities, and opacities. The synthetic spectra thus obtained are compared with the observed spectra for each iteration. The procedure is automated and requires only initial input parameters with user-defined ranges for each parameter to constrain the parameter space physically. SYNAPPS has been predominantly used to model stripped-envelope and thermonuclear SNe spectra but has been successfully utilized in a number of hydrogen-rich

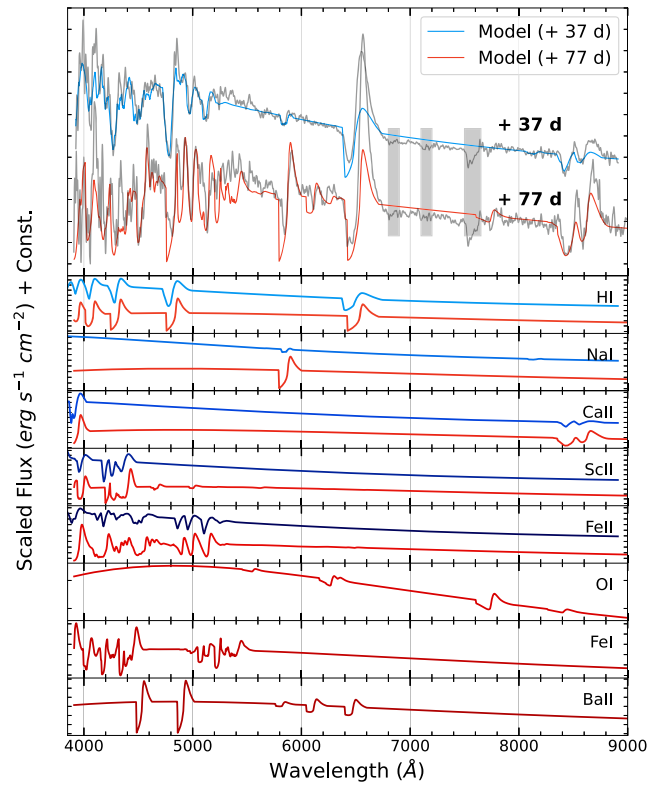


Figure 5. SYNAPPS model fitting to the observed spectra around the mid- and end-plateau phases. The lower small panels show the model spectra of individual species when the contribution from rest of the species is turned off.

SNe cases as well (Takáts & Vinkó 2012; Sahu et al. 2013; Bostroem et al. 2019; Dastidar et al. 2021).

For the first setup to model the +37 days spectrum, we include only five species, namely H I, Ca II, Na I, Sc II, and Fe II. The overall best-fit spectra and various species contributions are shown in Figure 5. The individual species contributions are obtained by utilizing the best-fit output as input in `syn++` by turning on one species at a time in the input file. No warping function is applied, i.e., $a1 = a2 = 0$. Only $a0$ is varied, which signifies the flux level. Photospheric velocity obtained on the day +37 days is 3830 km s^{-1} .

For end-plateau spectra at +77 days, in addition to the previously included species, we add three more metal species, namely Ba II, Fe I, and O I. Further, we find that the broad emission band around 4800 Å is a blend of multiple metal lines originating from neutral Fe, Sc II, and Ba II. The photospheric velocity obtained from these fits around +77 days is 2170 km s^{-1} .

In Figure 6, we compare the SN 2021wvw spectra with a few other short-plateau SNe along with the low-luminosity SN 2005cs and intermediate-luminosity SN 2021gmj. First, in the top panel of Figure 6, we compare the spectra around 20 days when the metal features are well developed. We clearly observe that there are similarities as well as dissimilarities in the spectral features. At first glance, the features appear similar to SN 2005cs and SN 2021gmj, i.e., narrow and strong absorption. The $H\alpha$ absorption appears shallow, which seems to be the general trend for the short-plateau SNe and is completely indiscernible in some of the brighter and fast-declining short-plateau SNe, e.g., SN 2006Y, SN 2006ai, and SN 2016gez. At similar epochs, other SNe have well-developed metal features such as Fe II lines toward the blue end, whereas

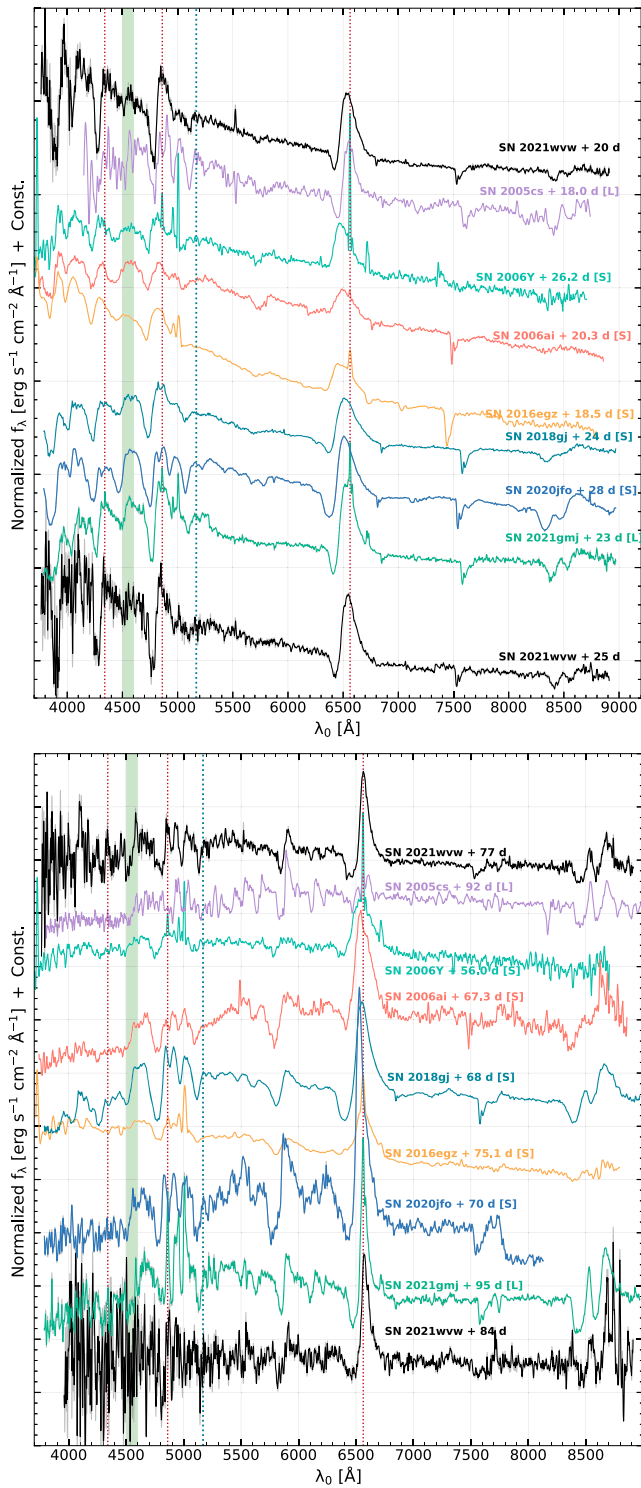


Figure 6. Spectral comparisons at the early- and late-plateau phase with short-plateau SNe and with other subluminal SNe.

we only see a hint of these lines in SN 2021wvw. In the bottom panel of the same figure, we compare SN 2021wvw spectra during the end-plateau phase, where we find the appearance of the strongest metallic features. Comparison spectra for other SNe are taken at similar epochs. The SN 2021wvw spectra show similar features to other subluminal SNe, but the absorption depths are shallow. However, SN 2021wvw has well-developed P-Cygni (more representative of a typical Type

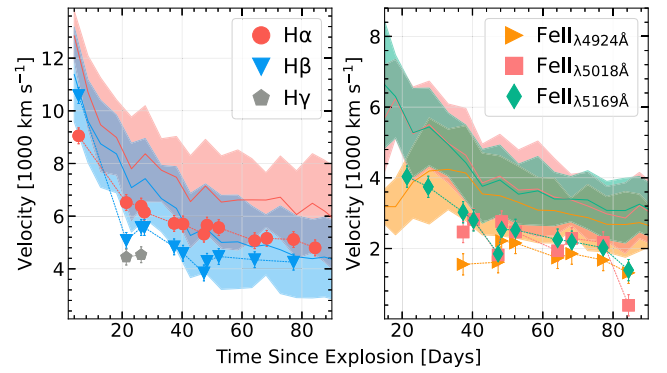


Figure 7. Expansion velocity evolution estimated from several prominent metallic features (including Balmer lines) observed in the spectra. The velocities have been compared with a large sample taken from Gutiérrez et al. (2017). The shaded region gives the corresponding 1σ scatter around the sample mean.

IIP) profiles compared to much shallower absorption depths in short-plateau SNe SN 2006Y, SN 2006ai, and SN 2016egz.

4.2. Velocities

We utilize some of the well-resolved absorption features to estimate expansion velocities of the ejecta. We iteratively measure the absorption minimum of these lines using IRAF by fitting an inverted Gaussian assuming a multitude of continuum points. The absorption minima are corrected for redshift and eventually converted to the expansion velocities using the central rest wavelengths of the corresponding features. We have estimated these velocities for six lines as shown in Figure 7. The errors in velocity estimates are much smaller than the instrumental resolution; hence, the latter has been quoted as the errors in the velocities.

For the first epoch (+5.5 days), we could identify the absorption dips blueward of H α and H β rest wavelengths corresponding to $\sim 9100 \text{ km s}^{-1}$ and $\sim 10,600 \text{ km s}^{-1}$ line velocity, respectively. At +21 days, apart from Balmer features, we could measure the velocity from Fe II 5169 Å. Up to +85 days, the velocities are measured, and their time evolution is shown in Figure 7. Around +40 days, which is proximal to the midplateau mark, we measure the H α and Fe II 5169 Å velocities as $\sim 5700 \text{ km s}^{-1}$ and $\sim 2800 \text{ km s}^{-1}$, respectively. The SYNAPPS modeling around similar phase gives a value which is between these two values ($\sim 3830 \text{ km s}^{-1}$). As the ejecta evolves, the expansion velocities keep decreasing until we can confidently resolve the absorption minimum. Toward the end of the plateau phase, around +75 days, we find the expansion velocities to be $\sim 2000 \text{ km s}^{-1}$ from Fe lines and $\sim 5100 \text{ km s}^{-1}$ from H α . The model spectrum around a similar phase gives $\sim 2170 \text{ km s}^{-1}$ as the photospheric velocity, which is much closer to the values obtained from the metallic features.

We further compare these velocities with the mean expansion velocities obtained from a larger sample of Type II SNe (Gutiérrez et al. 2017). The mean velocities and 1σ scatter in these are overplotted in Figure 7. We see that the SN 2021wvw velocities lie at the lower 1σ end of the sample, implying that this is a slowly evolving ejecta. For metal lines, the velocities are even smaller than the lower 1σ edge from the sample. Around midplateau, the difference between the mean velocities of the sample and SN 2021wvw observed velocities is $\sim 1500 \text{ km s}^{-1}$.

Table 3
Core Parameters for Best-matching Semianalytical Models

Parameters ^a	$R = 300 M_{\odot}$	$R = 500 M_{\odot}$	$R = 700 M_{\odot}$
$M_{\text{ej}} (M_{\odot})$	$6.50^{+0.20}_{-0.20}$	$6.20^{+0.20}_{-0.05}$	$6.60^{+0.10}_{-0.10}$
$E_{\text{th}} (10^{51} \text{ erg})$	$0.27^{+0.13}_{-0.05}$	$0.17^{+0.04}_{-0.04}$	$0.12^{+0.03}_{-0.02}$
$E_{\text{kin}} (10^{51} \text{ erg})$	$1.00^{+0.20}_{-0.12}$	$0.93^{+0.03}_{-0.02}$	$1.05^{+0.01}_{-0.01}$
$M_{\text{Ni}} (M_{\odot})$	$0.020^{+0.004}_{-0.006}$	$0.020^{+0.004}_{-0.005}$	$0.020^{+0.004}_{-0.005}$

Note.

^a $T_{\text{rec}} \approx 6000 \text{ K}$, $A_{\text{g}} = 6.5 \times 10^{10} \text{ days}^2$.

5. Plausible Progenitor

5.1. Semianalytical Models

We attempt to model the bolometric light curve of SN 2021wvw using a two-component progenitor model (Nagy & Vinkó 2016) to roughly constrain a few parameters and motivate detailed modeling. This formulation comprises of a dense “core” and an extended “envelope,” representing the bulk of the ejecta and the near-surface layers, respectively. Arnett & Fu (1989) form the basis of this semianalytical formulation with subsequent additions by Blinnikov & Popov (1993); Nagy et al. (2014) to obtain approximate ejecta mass (M_{ej}), progenitor radius (R_0), energy (E_{tot}), and ^{56}Ni mass (M_{Ni}) estimates. The total energy E_{tot} comprises ejecta kinetic energy (E_{k}) and initial thermal energy (E_{th}) deposited by the shock ($E_{\text{tot}} = E_{\text{k}} + E_{\text{th}}$). In this analytical formulation, the SN ejecta, which is spherically symmetric, is divided into two components: (a) an interior core with a constant (or flat) density; and (b) an outer less dense shell with an exponential ($n = 2$) density profile (Nagy & Vinkó 2016). These components have independent sets of physical parameters, with the origin of the radius being the same. The contribution from each component to the light curve is estimated independently.

There is a degeneracy among various parameters (Nagy & Vinkó 2016). In a similar analysis for two other short-plateau SNe, SN 2018gj and SN 2020jfo, the progenitor radii did not match well with the results obtained using detailed hydrodynamical modeling (Teja et al. 2022, 2023a). So, in this work we do not attempt to constrain the radius of the progenitor; instead, we fix the radius to multiple values beforehand. We take three cases: a fairly compact progenitor ($300 R_{\odot}$), a typical RSG radius ($700 R_{\odot}$), and a radius in between ($500 R_{\odot}$). We vary other parameters to get a light curve matching the observed light curve. Another caveat to consider is the lack of early UV and U -band data, which, in models, is usually governed by the shell part. This outer envelope could also act as proximal CSM around the RSG progenitor (Nagy & Vinkó 2016). Due to lack of data, no attempts were made to estimate CSM. Instead, we fixed the shell values (to a negligible contribution) so that they do not affect the early light curve. Since the models are analytical, the errors are estimated by first obtaining a match to the observed light-curve data, followed by varying the parameters to fit the upper and lower error bars associated with the observed light curve. The best parameters obtained for the fixed radii values are presented in Table 3. We could find that the model fits equally well with very similar parameters within error bars for each radii value. The case for $500 R_{\odot}$ is shown in Figure 8.

The best-fit values of the parameters M_{ej} and M_{Ni} do not vary much for the different radii considered here. The only

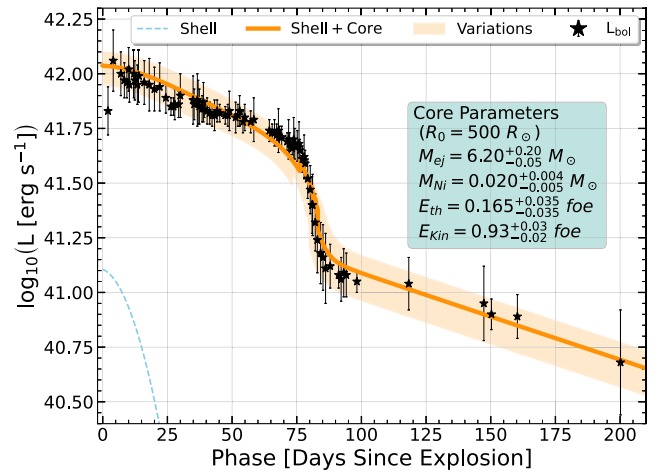


Figure 8. Semianalytical fit for fixed radii of $500 R_{\odot}$. The values provided in the inset are for the best-matching models.

considerable changes are in the energy values. From these models, we find the M_{ej} to be $\sim 6.5 M_{\odot}$, $M_{\text{Ni}} = 0.020 \pm 0.005 M_{\odot}$, and a total energy between 1.1 and 1.3 foe. The M_{ej} values for SN 2021wvw are similar to those obtained in other short-plateau cases (e.g., SN 2018gj, SN 2020jfo) but with lower explosion energy. The lower energy values are expected for SN 2021wvw, considering its subluminous nature. The total energy contribution from the core in the case of low-luminosity SN 2005cs is ~ 0.5 foe (Nagy & Vinkó 2016) with $M_{\text{ej}} = 8.0 M_{\odot}$. Considering the intermediate brightness of SN 2021wvw and a shorter plateau length, the estimated parameters are reasonably well constrained with tight bounds on the ^{56}Ni mass. Using these values as our reference point, we delve into more details about the progenitor and its origins using complete hydrodynamical modeling.

5.2. Hydrodynamical Modeling

In the previous section, we obtained rough estimates of the progenitor parameters. Unfortunately, we lack the nebular phase spectra, which could also be utilized to constrain the progenitor’s C/O core mass. Initially, we looked for models representative of SN 2021wvw evolution in other previous studies. However, none of the grids of model light curves or individual models available in the literature could provide a short-plateau length with low luminosity (Dessart et al. 2010; Eldridge et al. 2018; Moriya et al. 2023). For the case of short-plateau SNe, it has been noticed that a wide range of plausible RSG masses could give rise to these SNe ranging from 8 to $12 M_{\odot}$ (Sollerman et al. 2021; Teja et al. 2022; Utrobin & Chugai 2024) and reaching up to 20–30 M_{\odot} (Dessart et al. 2010; Hiramatsu et al. 2021). Therefore, to ascertain the properties of the plausible progenitor of SN 2021wvw, its evolutionary scenario, mass loss before the explosion, explosion energy, and ejecta mass, we perform the hydrodynamical modeling by evolving progenitors for both the lower and higher end of RSGs, allowing arbitrarily enhanced winds to mimic the impact of prior mass loss (due to binary interaction (e.g., Laplace et al. 2021; Ercolino et al. 2024) or eruptive mass loss during the star’s life (e.g., Cheng et al. 2024) on the mass of the H-rich ejecta.

We use the 1D stellar evolution code MESA (Paxton et al. 2011, 2013, 2015, 2018, 2019; Jermyn et al. 2023) revision

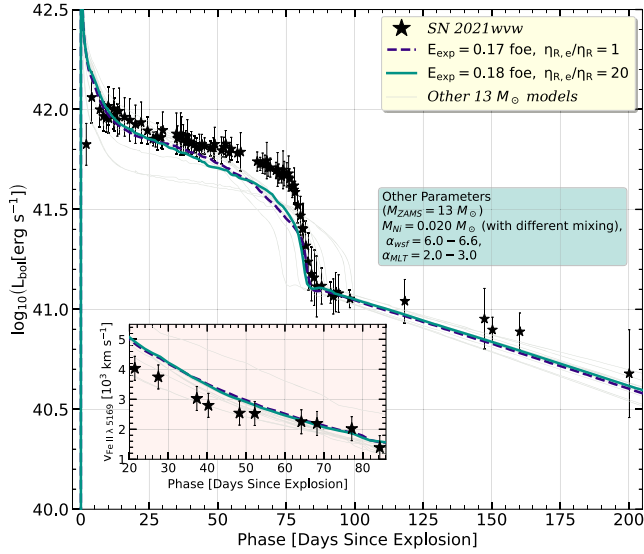


Figure 9. Observed and modeled bolometric evolution of SN 2021wvw for $13 M_{\odot}$ ZAMS models with different sets of parameters. The inset in the left-hand bottom corner shows the corresponding modeled and observed Fe II 5169 velocities.

15140 to evolve the progenitor and hydrodynamical explosion and STELLA (Blinnikov & Sorokina 2004; Baklanov et al. 2005; Blinnikov et al. 2006) to obtain synthetic observables, specifically light curves and expansion velocity. Most of the parameters in MESA were kept the same as provided in the inlists `make_pre_ccsn_IIP` and `ccsn_IIP` and described in detail in Farmer et al. (2016) and Paxton et al. (2018); additional detailed descriptions of the setup and key parameters are mentioned in Teja et al. (2022, 2023a). We use the binding-energy fallback scheme introduced in Goldberg et al. (2019) and Paxton et al. (2019) to quantify late-time fallback during the shock-propagation phase. In this work, we mainly focus on the following parameters: zero-age main-sequence (ZAMS) mass, metallicity (z), wind scaling factor (α_{wsf}), mixing length (α_{MLT}), explosion energy, nickel mass, and explosive mixing via the Duffell Rayleigh–Taylor instability (RTI; Duffell 2016) 1D implementation by varying the ratio of RTI parameter $\eta_{R,e}$ and diffusion parameter η_R (Paxton et al. 2018). The progenitor models are exploded in MESA via a thermal energy injection to a specified total explosion energy, and the ejecta evolution is followed to just before shock breakout (SB) following Paxton et al. (2018) as discussed in Teja et al. (2022, 2023a) making use of the Duffell (2016) implementation for mixing via the RTI. The models are then handed off to STELLA when the shock reaches an overhead mass coordinate of $0.05 M_{\odot}$. Before evolving a new set of progenitors, we first try the short-plateau models from previous works, namely SN 2020jfo (Teja et al. 2022) and SN 2018gj (Teja et al. 2023a). Exploding these with lower energies to match the plateau luminosities makes the plateau length longer, leaving these models infructuous. We then proceed to evolve additional models.

First, we evolve $13 M_{\odot}$ ZAMS mass models with solar metallicity for the lower-mass end. We change the wind scaling (α_{wsf}) in steps and explode each progenitor with various explosion energies until we match the plateau luminosity and its duration. Some of the resulting bolometric light curves and corresponding Fe II 5169 velocities are presented in Figure 9, which are compared with the observed values. As stated earlier, we do not attempt to match the initial

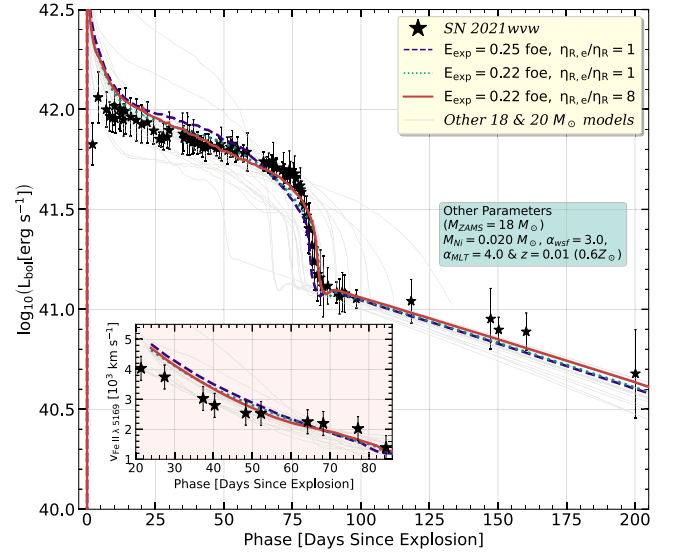


Figure 10. Observed and modeled bolometric evolution of SN 2021wvw for $18 M_{\odot}$ ZAMS models with different sets of parameters. The solid red curve gives the best description of the model. The inset in the bottom left-hand corner shows the corresponding modeled and observed Fe II 5169 velocities.

10–20 days of observations exactly with models due to lack of relevant observations. We find that the velocities, plateau luminosity, and nickel tail match reasonably well for low-mass RSG models. However, these models could not reproduce the observed slow decline during the plateau phase and the sharp transition from the plateau to the tail phase. A sharp decline for SN 2005cs was obtained by increasing the strength of RTI mixing, as shown in Paxton et al. (2018). As a more thoroughly mixed ejecta is expected to cause a steeper plateau drop due to a more even distribution of H throughout the entire ejecta, we also attempt to vary the RTI mixing via $\eta_{R,e}/\eta_R$, which directly changes the density structure as well as the abundance structure of the progenitor and the varied degree of mixing of species. Even for a value as high as $\eta_{R,e}/\eta_R = 20$, we only observe slight changes in the model light curves, but not significant enough to satisfy the observed transition (refer Figure 9).

We proceed further to explore and explode the higher ZAMS mass models in the range $18\text{--}20 M_{\odot}$, which plausibly lie on the upper mass limit for the directly detected progenitors of Type II SNe (Smartt et al. 2009; Davies & Beasor 2020). The resulting models are shown in Figure 10 with colored lines representing the best match to the observations (other models are in gray color). Owing to their large progenitor radii ($\sim 1000 R_{\odot}$) at the mixing length $\alpha_{\text{MLT}} = 2$, the initial models were too bright to fit the plateau luminosities, even with very low explosion energies. Hence, we evolved slightly compact progenitors to match the plateau decline and luminosities by varying the α_{MLT} and metallicity z . For $\alpha_{\text{MLT}} = 4.0$ and $z = 0.6Z_{\odot}$, we could obtain a considerable match with the observed light curves for explosion energies of $\approx 0.22\text{--}0.25$ foe with $M_{\text{ej}} = 4.7 M_{\odot}$. This value of α_{MLT} is on the higher end of typically considered values (see, e.g., Goldberg & Bildsten 2020), and is consistent with 3D simulations of convective RSG envelopes (Goldberg et al. 2022). The transition to the end of the plateau obtained for these models is inherently sharp, which is further matched well by varying the RTI parameter. We could replicate the observed transition profile for $\eta_{R,e}/\eta_R = 8$. The mass of ^{56}Ni required to

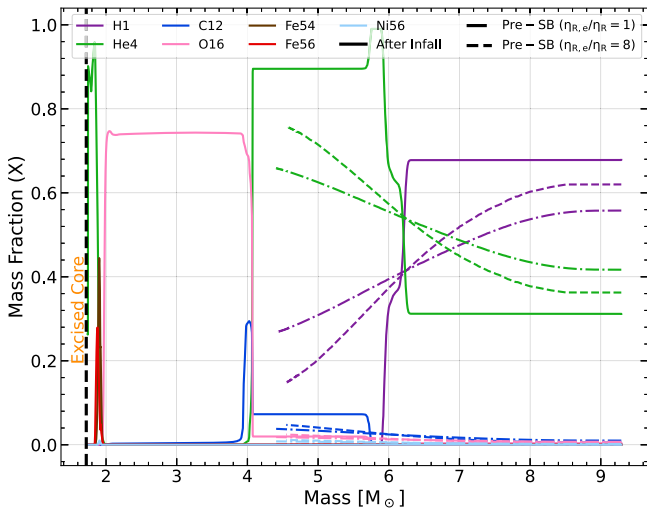


Figure 11. MESA+STELLA structures for different cases of $18 M_{\odot}$ ZAMS models with different RTI parameters. A few species out of the 22 species network used in the modeling are shown here. Solid lines present the mass fraction just after we inject the explosion energy. The other two dashed lines show the final ejecta structure before the SB for different $\eta_{R,e}/\eta_R$ values. The final ejecta profiles suffer from significant fallback during the shock-propagation phase, which we discuss in Section 6.2.

fit the observed light curve is similar to the earlier estimates with $M_{\text{Ni}} \approx 0.020 M_{\odot}$. The ejecta mass and explosion energies obtained through hydrodynamical modeling are lower than that obtained from the semianalytical approach. However, such discrepancies between semianalytical and detailed modeling are fairly common in the literature (see for example, Szalai et al. 2019; Teja et al. 2023a). This could be due to various simplified approximations in the semianalytical work, including the assumed density and velocity profile of the ejecta, as well as the assumption of a simple two-zone ejecta with a gray opacity treatment independent of metallicity (Nagy & Vinkó 2016).

We show the structural differences in the various models considering the effect of the RTI parameter in Figure 11 using a few species out of the 22 species network used in the modeling. Solid lines represent the mass fraction just after we inject the explosion energy. The other two dashed lines show the final ejecta structure before the SB for different $\eta_{R,e}/\eta_R$ values. The figure shows that the higher η ratio weakens the RTI mixing with increasing species concentration toward the inner layers. At the boundary interface, the gradient is steeper for a higher η ratio. Due to the small explosion energies, the models experience significant fallback during the shock-propagation phase as reverse shocks off the steep density gradients at various compositional boundaries sweep marginally unbound material back onto the inner boundary. This is also evident in Figure 11, where the inner boundary of the final pre-SB structure is at a significantly higher mass coordinate ($\approx 4.5 M_{\odot}$) than what was initially excised as a core remnant mass ($\approx 1.7 M_{\odot}$). The detailed fallback treatment in MESA is described in Goldberg et al. (2019). Due to the relatively low core binding energy in the suite of $13 M_{\odot}$ progenitors, we find only $0.2\text{--}0.4 M_{\odot}$ of material is falling onto the core in $13 M_{\odot}$ progenitor case, whereas it is much larger for high-mass scenarios reaching up to $2\text{--}3 M_{\odot}$ (owing to the larger core binding energy of the high-mass progenitors). Approximately $1 M_{\odot}$ of fallback was also present in the SN 2005cs models (Paxton et al. 2018), even for an initial low-mass progenitor ($13 M_{\odot}$).

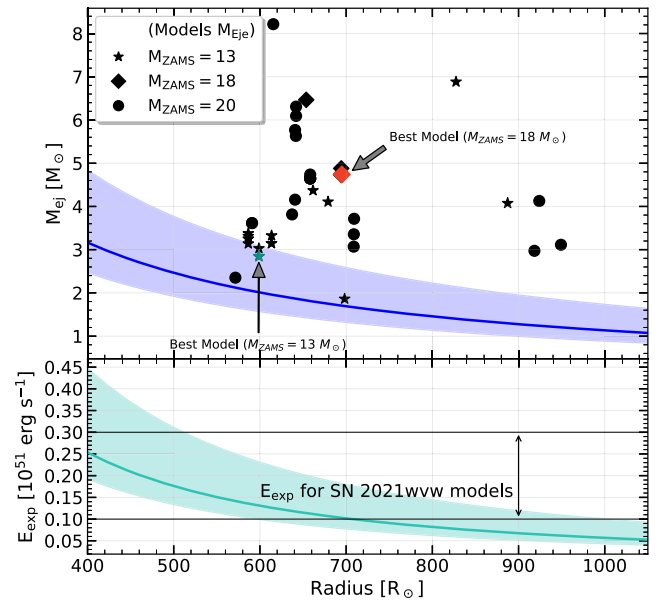


Figure 12. Plausible E_{exp} and M_{ej} ranges plotted from the scaling relations obtained in Goldberg et al. (2019). The scatter points represent the ejecta masses obtained for various models utilized in this work. The energy values for all the evolved models are between 0.1 and 0.3 foe. The shaded regions include the values obtained considering the errors in the observables.

6. Discussion

6.1. Scaling Relation Degeneracies and Model Differences for Short-plateau SNe

Many works have highlighted the nonuniqueness of hydrodynamical modeling of SN-IIP light curves and plateau velocities (Dessart & Hillier 2019; Goldberg et al. 2019; Martinez & Bersten 2019; Goldberg & Bildsten 2020). Semianalytical scalings between luminosity and plateau duration with progenitor properties thus entail families of explosions which may produce qualitatively similar light curves, with higher M_{ej} and E_{exp} at lower R being comparable to smaller M_{ej} and E_{exp} at higher R (Popov 1993; Kasen & Woosley 2009; Sukhbold et al. 2016; Goldberg et al. 2019; Goldberg & Bildsten 2020). We compare a selection of our MESA models (from Section 5) to the scaling relations obtained by Goldberg et al. (2019) to estimate a comprehensive set of ejecta mass and explosion energies, shown in Figure 12. We note that these scaling relations were calibrated to higher Ni masses and more typical (i.e., less stripped) events. We do not take these scaling relations as the absolute truth in this regime, but rather show them as representative of the degeneracies characteristic of SNe IIP (Dessart & Hillier 2019; Goldberg et al. 2019; Goldberg & Bildsten 2020), and use them to motivate and contextualize our hydrodynamical modeling efforts. For radii between 400 and $1000 R_{\odot}$, we find the explosion energy varies from $\approx 2.5 \times 10^{50} \text{ erg s}^{-1}$ to much lower $5 \times 10^{49} \text{ erg s}^{-1}$.

For the given radii range, the predicted ejecta masses are less than $3 M_{\odot}$. The modeled ejecta masses lie somewhat above the values obtained utilizing scaling relations for all the progenitors, possibly due to the smaller ratio of core mass to envelope mass in the sample used to calibrate the scalings compared to the models presented here. The explosion energy provides good matching values. These relations tend to give similar values obtained by semianalytical modeling for the much more

compact radii ($<400 R_{\odot}$), also seen in the case of another short-plateau SN 2018gj (Teja et al. 2023a).

In both the low- and high-mass cases for SN 2021wvw, we find apparent differences in the early phase (<40 days) modeled and observed velocities. The differences are significant in the $13 M_{\odot}$ models. This tension is further increased in low-mass models when we try to match the observed plateau luminosity by increasing their progenitor radius. In other modeling works, it has been noted that the MESA+STELLA models provide an excellent velocity match with typical Type IIP SNe observed velocities from the early phase until the photospheric phase, which is not the case for the short-plateau events.

6.2. Fallback during the Shock-propagation Phase

In a majority of the modeled subluminous SNe that are the result of low-energy explosions, whether they come from low-to moderate-mass ($8\text{--}18 M_{\odot}$) RSGs (Chugai & Utrobin 2000; Pumo et al. 2017; Lisakov et al. 2018; Valerin et al. 2022) or high-mass RSG explosions ($>20 M_{\odot}$ Zampieri et al. 2003), there are discussions related to fallback material onto the core. Namely, when the total explosion energy is positive but only comparable in magnitude to the total binding energy of the progenitor star, late-time fallback from reverse shocks during the pre-SBO phase may sweep marginally unbound material back onto the central remnant (see, e.g., Colgate 1971; Perna et al. 2014). In some cases, the central remnant has been speculated to turn into a black hole postaccretion, but with no observational evidence (Zampieri et al. 2003). In other cases, very late-time enhanced luminosity is associated with the accretion of material to the central remnant (Gutiérrez et al. 2020). For many of these objects, the ^{56}Ni mass obtained is an order of magnitude or even much lesser than the ^{56}Ni mass obtained for SN 2021wvw. Further, the velocity obtained for these cases is much less than the usual Type II expansion velocities.

Interestingly, the short plateau and a sharp transition to the plateau phase are remarkable features for SN 2021wvw, which are unusual for low to intermediate-luminosity SNe. Given the low inferred E_{exp} , the short-plateau length requires a low H-rich ejecta mass for both low-mass and high-mass progenitors, which could be the result of a higher mass loss during evolution. Such high mass loss might be consistent with the notion that the sharp drop from the plateau is actually *excess* luminosity during the plateau drop driven by late-time interaction with previously ejected material. But, as observed in the spectral evolution (Section 4), there are no discernible CSM signatures in the spectra. On the other hand, if there is an actual fallback (as occurs during hydrodynamical modeling in Section 5) of the inner layers onto the core, the inward receding photosphere may reach earlier to the base of the H-rich ejecta, giving a short plateau with a sharp transition. This may manifest in late-time signatures of accretion if such accretion persists (see, e.g., Dexter & Kasen 2013; Moriya et al. 2019). However, the lack of late-time light curve (beyond 300 days) and spectral information restricts us from saying anything about further observational signatures of fallback accretion.

While the short plateau and its sharp transition could be due to fallback, further discussion of the physical consequences of this fallback and ascertaining its influence on the sharp transition from plateau requires further detailed modeling, which is beyond the scope of this work. We nonetheless encourage

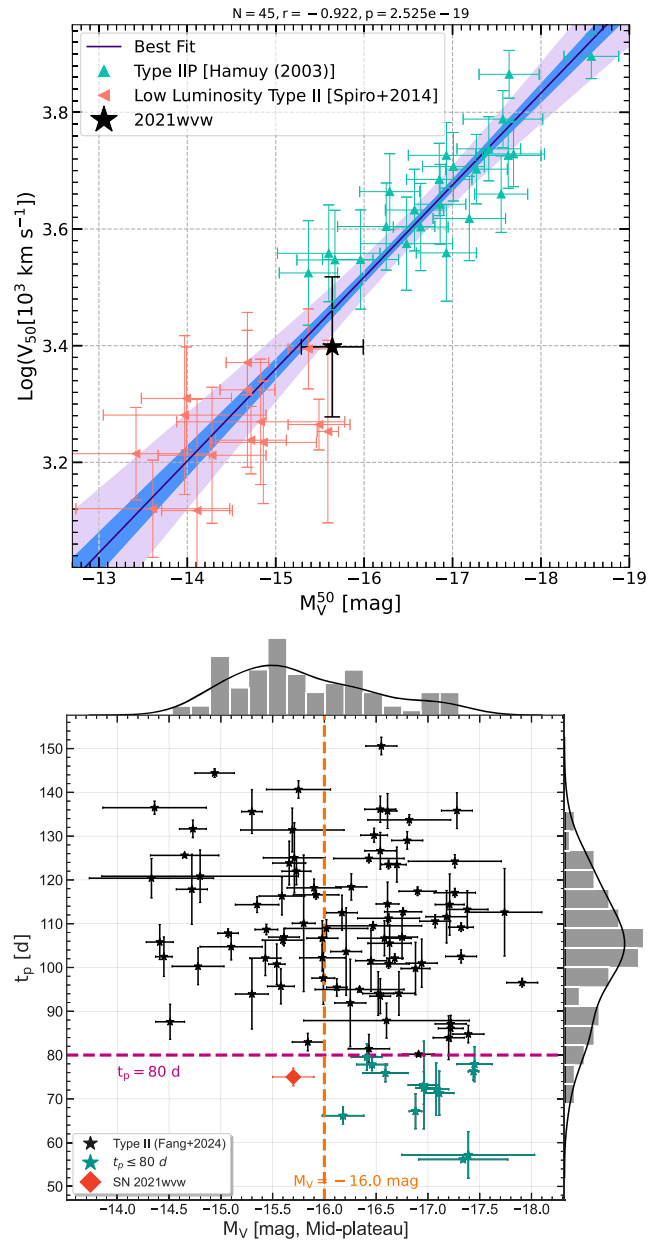


Figure 13. Top panel: correlation between plateau brightness at 50 days, M_V^{50} and expansion velocities at 50 days after explosion. Bottom panel: midplateau brightness, M_V vs. plateau duration (t_p) for a large sample including a wide range of Type II SNe obtained from Fang et al. (2024).

follow-up observations searching for any signatures of continued accretion or very late-time circumstellar interaction from this unique event.

6.3. SN 2021wvw in the Type II Domain

We compare SN 2021wvw with a large sample of normal Type IIP SNe (Hamuy 2003) and low-luminosity Type II SNe (Spiro et al. 2014) as shown in Figure 13. SN 2021wvw fits well in the established tight correlation between expansion velocity and luminosity for Type II SNe at 50 days. Moreover, we find it bifurcating the two populations in both luminosity and expansion velocities. In this space, it is a bridging object between the normal Type IIP SNe and underluminous ones. Apart from this expected behavior, SN 2021wvw is unique due

to its short plateau and low luminosity. Considering existing works (e.g., Figure 17 in Valenti et al. 2016) showing a correlation between plateau luminosity and plateau duration, SN 2021wvw is clearly an outlier. Even for a larger sample for all Type II subclasses (Fang et al. 2024), SN 2021wvw stands apart, as is evident in the bottom panel of Figure 13. SN 2021wvw has the shortest plateau among all the intermediate and low-luminosity SNe. In contrast, it is the faintest SN among all the short-plateau subclass of Type IIP SNe presented in the sample and, presumably, in the literature.

7. Summary

This work provides a comprehensive set of multiband photometric and optical spectroscopic observations of an underluminous, short-plateau supernova SN 2021wvw. We have presented detailed light curves and spectral comparisons with other short-plateau SNe. The light curves and spectra are modeled to obtain the physical parameters of the explosion. Some of the key findings are summarized as follows:

1. SN 2021wvw is fainter (at $M_r \approx -16$ mag) compared with other short-plateau SNe and shows the shortest plateau (≈ 75 days) among the intermediate-luminosity SNe, with a sharp transition period of ~ 10 days from plateau to tail phase.
2. The ejecta expansion velocities are slowly evolving and lie below the 1σ lower bound compared to a large sample of Type II SNe.
3. Early spectra show fewer metallic features as compared to other short-plateau and subluminous SNe. The lack of metal features is evident until the last spectrum (+95 days) presented here.
4. Detailed MESA+STELLA hydrodynamical modeling disfavors the lower mass RSG models and is more inclined toward the higher mass end of RSGs. A compact progenitor with $18 M_\odot$ ZAMS mass, radius of $650\text{--}700 R_\odot$ and a final H-rich ejecta mass of $\approx 5 M_\odot$ is seen to provide a good fit to the observed properties.
5. Modeling also suggests a low explosion energy ($\approx 0.23 \times 10^{51}$ erg) with an estimated $0.020 M_\odot$ of radioactive ^{56}Ni .

With the increasing number of short-plateau SNe, we find that these events have varied luminosities, synthesized ^{56}Ni masses, and expansion velocities. It is evident that these are not restricted to moderate to luminous events, as seen previously. With the upcoming large surveys such as LSST, this number would only increase and possibly make the Type IIP class or subclasses more homogenous in different parameter spaces.

Acknowledgments

We are grateful to the anonymous referee for thoroughly evaluating the manuscript, which helped improve it.

R.S.T. would like to acknowledge Dr. Takashi J. Moriya for his insights and helpful discussions on this supernova.

R.S.T. and J.A.G. thank Dr. Daichi Hiramatsu for readily providing observational data for a few short-plateau SNe, as well as for valuable discussions.

D.K.S. acknowledges the support provided by DST-JSPS under grant No. DST/INT/JSPS/P 363/2022.

G.C.A. thanks the Indian National Science Academy for support under the INSA Senior Scientist Programme.

The Flatiron Institute is supported by the Simons Foundation.

The GROWTH India Telescope (GIT) is a 70 cm telescope with a 0.7° field of view, set up by the Indian Institute of Astrophysics (IIA) and the Indian Institute of Technology Bombay (IITB) with funding from Indo-US Science and Technology Forum and the Science and Engineering Research Board, Department of Science and Technology, Government of India. It is located at the Indian Astronomical Observatory (IAO, Hanle). We acknowledge funding by the IITB alumni batch of 1994, which partially supports the operation of the telescope.

We thank the staff of IAO, Hanle, CREST, and Hosakote, who made these observations possible. The facilities at IAO and CREST are operated by the Indian Institute of Astrophysics, Bangalore.

This research has made use of the high-performance computing (HPC) resources at <https://www.iiap.res.in/?q=facilities/computing/nova> made available by the Computer Center of the Indian Institute of Astrophysics, Bangalore.

This work has made use of data from the Asteroid Terrestrial-impact Last Alert System (ATLAS) project. The Asteroid Terrestrial-impact Last Alert System (ATLAS) project is primarily funded to search for near-Earth asteroids through NASA grants NN12AR55G, 80NSSC18K0284, and 80NSSC18K1575; byproducts of the NEO search include images and catalogs from the survey area. This work was partially funded by Kepler/K2 grant J1944/80NSSC19K0112 and HST GO-15889, and STFC grants ST/T000198/1 and ST/S006109/1. The ATLAS science products have been made possible through the contributions of the University of Hawaii Institute for Astronomy, the Queen's University Belfast, the Space Telescope Science Institute, the South African Astronomical Observatory, and The Millennium Institute of Astrophysics (MAS), Chile.

This research has made use of the NASA/IPAC Extragalactic Database (NED), which is funded by the National Aeronautics and Space Administration and operated by the California Institute of Technology.

This research has made use of the NASA/IPAC Infrared Science Archive, which is funded by the National Aeronautics and Space Administration and operated by the California Institute of Technology.

Facilities: HCT, GIT, ATLAS

Software: astropy (Astropy Collaboration et al. 2013, 2018, 2022), ds9 (Smithsonian Astrophysical Observatory 2000), emcee (Foreman-Mackey et al. 2013), IRAF (Tody 1993), Jupyter-notebook (Kluyver et al. 2016), matplotlib (Hunter 2007), MESA, numpy (Harris et al. 2020), pandas (McKinney 2010; pandas development team 2020), plot_atlas_fp.py (Young 2020), scipy (Virtanen et al. 2020), STELLA, SYNAPPS.

Appendix Data

The following section provides the apparent magnitudes obtained for SN 2021wvw. The magnitudes are given in Table 4.





Table 4
Photometric Observations of SN 2021www from GIT and HCT

JD (2459000+)	Phase ^a (days)	<i>g</i> (mag)	<i>V</i> (mag)	<i>r</i> (mag)	<i>R</i> (mag)	<i>i</i> (mag)	<i>z</i> (mag)
458.3	8.4	18.07 ± 0.18	...	17.68 ± 0.09	...	17.72 ± 0.11	...
459.3	9.4	18.10 ± 0.12	...	17.68 ± 0.08	...	17.65 ± 0.11	17.45 ± 0.11
460.2	10.3	18.11 ± 0.15	...	17.65 ± 0.10	...	17.64 ± 0.14	...
462.3	12.4	17.66 ± 0.05	...	17.63 ± 0.06	...
463.3	13.4	18.12 ± 0.10	...	17.67 ± 0.05	17.36 ± 0.13
465.3	15.4	18.17 ± 0.10
471.3	21.4	17.40 ± 0.18
474.3	24.4	18.30 ± 0.16	...	17.69 ± 0.08	...	17.66 ± 0.07	17.44 ± 0.10
476.3	26.4	18.40 ± 0.12	18.06 ± 0.01	17.81 ± 0.05	17.56 ± 0.01	17.64 ± 0.06	...
477.3	27.4	...	18.05 ± 0.01	17.79 ± 0.06	17.55 ± 0.02	17.64 ± 0.07	17.49 ± 0.09
478.2	28.3	17.62 ± 0.12	...
479.3	29.4	17.80 ± 0.06	...	17.70 ± 0.08	...
485.3	35.4	17.76 ± 0.05	...	17.66 ± 0.06	...
486.3	36.4	18.49 ± 0.11	...	17.65 ± 0.05	...	17.63 ± 0.08	17.56 ± 0.12
487.3	37.4	17.75 ± 0.06	...	17.69 ± 0.07	17.51 ± 0.11
488.4	38.5	18.53 ± 0.15	...	17.75 ± 0.09	...	17.67 ± 0.08	...
489.2	39.3	18.51 ± 0.14	...	17.76 ± 0.09	...	17.61 ± 0.11	...
490.2	40.3	18.55 ± 0.14	18.07 ± 0.01	17.78 ± 0.06	17.56 ± 0.01	17.66 ± 0.09	...
491.3	41.4	18.58 ± 0.16	...	17.79 ± 0.08	...	17.61 ± 0.09	17.52 ± 0.11
492.2	42.3	18.62 ± 0.14	...	17.81 ± 0.11	...	17.68 ± 0.10	17.46 ± 0.11
493.3	43.4	18.62 ± 0.15	...	17.78 ± 0.09	...	17.72 ± 0.09	17.55 ± 0.12
494.2	44.3	18.54 ± 0.14	...	17.78 ± 0.09	...	17.66 ± 0.14	...
495.4	45.5	18.57 ± 0.15	...	17.81 ± 0.09	...	17.64 ± 0.11	17.56 ± 0.14
497.3	47.4	18.60 ± 0.15	...	17.83 ± 0.12	...	17.67 ± 0.13	17.53 ± 0.16
498.2	48.3	18.58 ± 0.12	...	17.81 ± 0.12	...	17.72 ± 0.09	...
501.3	51.4	18.72 ± 0.20	...	17.77 ± 0.12	17.61 ± 0.14
502.2	52.3	18.60 ± 0.14	...	17.84 ± 0.07	...	17.67 ± 0.08	...
503.2	53.3	18.51 ± 0.24
504.1	54.2	18.75 ± 0.13	...	17.92 ± 0.06	...	17.66 ± 0.07	17.56 ± 0.08
507.1	57.2	17.89 ± 0.08	...	17.63 ± 0.10	17.60 ± 0.12
508.3	58.4	17.75 ± 0.08	...	17.73 ± 0.10	17.66 ± 0.15
514.4	64.5	17.94 ± 0.13	17.69 ± 0.14
515.4	65.5	18.83 ± 0.16	...	18.05 ± 0.10	...	17.83 ± 0.11	...
516.3	66.4	17.93 ± 0.14	17.65 ± 0.21
517.2	67.3	18.04 ± 0.07	...	17.87 ± 0.08	...
518.3	68.4	18.89 ± 0.23	...	18.01 ± 0.16
519.1	69.2	18.06 ± 0.08	...	17.89 ± 0.08	...
521.2	71.3	18.85 ± 0.19	...	18.13 ± 0.11
522.2	72.3	18.94 ± 0.20	...	18.13 ± 0.11	...	17.98 ± 0.11	17.72 ± 0.13
523.2	73.3	18.21 ± 0.13
524.2	74.3	18.99 ± 0.16	...	18.12 ± 0.07	...	17.99 ± 0.10	17.81 ± 0.12
525.1	75.2	19.02 ± 0.18	...	18.13 ± 0.08	...	18.00 ± 0.09	...
526.2	76.3	19.03 ± 0.22	...	18.21 ± 0.13	17.84 ± 0.16
527.1	77.2	19.28 ± 0.19	...	18.29 ± 0.10
528.2	78.3	19.38 ± 0.24	...	18.29 ± 0.13	...	18.12 ± 0.14	17.94 ± 0.16
529.2	79.3	18.45 ± 0.14	...	18.18 ± 0.14	18.33 ± 0.20
530.1	80.2	19.70 ± 0.16	...	18.57 ± 0.09	...	18.35 ± 0.08	...
531.1	81.2	19.90 ± 0.11	...	18.79 ± 0.04	...	18.68 ± 0.06	...
532.1	82.2	19.04 ± 0.05
533.1	83.2	18.86 ± 0.07	...
534.1	84.2	19.38 ± 0.14	...	19.31 ± 0.11	...
535.1	85.2	19.52 ± 0.05	...	19.42 ± 0.08	...
536.1	86.2	19.73 ± 0.06
541.1	91.2	19.69 ± 0.08
542.1	92.2	19.85 ± 0.08
543.1	93.2	19.75 ± 0.07	...	19.50 ± 0.07	...
544.1	94.2	19.77 ± 0.07
548.2	98.3	19.78 ± 0.15
555.1	105.2	19.59 ± 0.17	...
563.1	113.2	19.64 ± 0.12	...
568.2	118.3	19.67 ± 0.08
575.0	125.1	...	20.95 ± 0.10	...	19.81 ± 0.05
580.0	130.1	...	21.17 ± 0.28

Table 4
(Continued)

JD (2459000+)	Phase ^a (days)	<i>g</i> (mag)	<i>V</i> (mag)	<i>r</i> (mag)	<i>R</i> (mag)	<i>i</i> (mag)	<i>z</i> (mag)
597.3	147.4	19.91 ± 0.10
600.2	150.3	20.21 ± 0.19
605.0	155.1	...	21.15 ± 0.26	...	20.19 ± 0.12
610.2	160.3	20.01 ± 0.24
625.0	175.1	...	21.19 ± 0.27	...	20.08 ± 0.10
626.2	176.3	20.97 ± 0.19
628.0	178.1	...	21.09 ± 0.12	...	20.44 ± 0.06
629.2	179.3	20.50 ± 0.23	...
636.0	186.1	...	21.03 ± 0.15
650.1	200.2	20.63 ± 0.12
665.0	215.1	...	21.65 ± 0.11	...	20.91 ± 0.10

Note.^a Phase given for $t_{\text{exp}} = 2459449.9$ JD.(This table is available in machine-readable form in the [online article](#).)**ORCID iDs**

Rishabh Singh Teja  <https://orcid.org/0000-0002-0525-0872>
 Jared A. Goldberg  <https://orcid.org/0000-0003-1012-3031>
 D. K. Sahu  <https://orcid.org/0000-0002-6688-0800>
 G. C. Anupama  <https://orcid.org/0000-0003-3533-7183>
 Avinash Singh  <https://orcid.org/0000-0003-2091-622X>
 Vishwajeet Swain  <https://orcid.org/0000-0002-7942-8477>
 Varun Bhalerao  <https://orcid.org/0000-0002-6112-7609>

References

- Anderson, J. P., González-Gaitán, S., Hamuy, M., et al. 2014, *ApJ*, **786**, 67
 Arnett, W. D., & Fu, A. 1989, *ApJ*, **340**, 396
 Astropy Collaboration, Robitaille, T. P., Tollerud, E. J., et al. 2013, *A&A*, **558**, A33
 Astropy Collaboration, Price-Whelan, A. M., Sipőcz, B. M., et al. 2018, *AJ*, **156**, 123
 Astropy Collaboration, Price-Whelan, A. M., Lim, P. L., et al. 2022, *ApJ*, **935**, 167
 Baklanov, P. V., Blinnikov, S. I., & Pavlyuk, N. N. 2005, *AstL*, **31**, 429
 Barbon, R., Ciatti, F., & Rosino, L. 1979, *A&A*, **72**, 287
 Bellm, E. C., Kulkarni, S. R., Graham, M. J., et al. 2019, *PASP*, **131**, 018002
 Blinnikov, S., & Sorokina, E. 2004, *Ap&SS*, **290**, 13
 Blinnikov, S. I., & Popov, D. V. 1993, *A&A*, **274**, 775
 Blinnikov, S. I., Röpke, F. K., Sorokina, E. I., et al. 2006, *A&A*, **453**, 229
 Bostroem, K. A., Valenti, S., Horesh, A., et al. 2019, *MNRAS*, **485**, 5120
 Cardelli, J. A., Clayton, G. C., & Mathis, J. S. 1989, *ApJ*, **345**, 245
 Cheng, S. J., Goldberg, J. A., Cantiello, M., et al. 2024, *ApJ*, in press (arXiv:2405.12274)
 Chugai, N. N., & Utrobin, V. P. 2000, *A&A*, **354**, 557
 Colgate, S. A. 1971, *ApJ*, **163**, 221
 Curtis, S., Wolfe, N., Fröhlich, C., et al. 2021, *ApJ*, **921**, 143
 Dastidar, R., Misra, K., Singh, M., et al. 2021, *MNRAS*, **504**, 1009
 Davies, B., & Beasor, E. R. 2020, *MNRAS*, **496**, L142
 Dessart, L., Gutiérrez, C. P., Ercolino, A., Jin, H., & Langer, N. 2024, *A&A*, **685**, A169
 Dessart, L., & Hillier, D. J. 2019, *A&A*, **625**, A9
 Dessart, L., Livne, E., & Waldman, R. 2010, *MNRAS*, **408**, 827
 Dexter, J., & Kasen, D. 2013, *ApJ*, **772**, 30
 Duffell, P. C. 2016, *ApJ*, **821**, 76
 Eldridge, J. J., Xiao, L., Stanway, E. R., Rodrigues, N., & Guo, N. Y. 2018, *PASA*, **35**, e049
 Ercolino, A., Jin, H., Langer, N., & Dessart, L. 2024, *A&A*, **685**, A58
 Fang, Q., Maeda, K., Ye, H., Moriya, T., & Matsumoto, T. 2024, arXiv:2404.01776
 Farmer, R., Fields, C. E., Petermann, I., et al. 2016, *ApJS*, **227**, 22
 Filippenko, A. V. 1997, *ARA&A*, **35**, 309
 Foreman-Mackey, D., Hogg, D. W., Lang, D., & Goodman, J. 2013, *PASP*, **125**, 306
 Förster, F., Cabrera-Vives, G., Castillo-Navarrete, E., et al. 2021, *AJ*, **161**, 242
 Goldberg, J. A., & Bildsten, L. 2020, *ApJL*, **895**, L45
 Goldberg, J. A., Bildsten, L., & Paxton, B. 2019, *ApJ*, **879**, 3
 Goldberg, J. A., Jiang, Y.-F., & Bildsten, L. 2022, *ApJ*, **933**, 164
 Gutiérrez, C. P., Anderson, J. P., Hamuy, M., et al. 2017, *ApJ*, **850**, 89
 Gutiérrez, C. P., Sullivan, M., Martínez, L., et al. 2020, *MNRAS*, **496**, 95
 Hamuy, M. 2003, *ApJ*, **582**, 905
 Harris, C. R., Millman, K. J., van der Walt, S. J., et al. 2020, *Natur*, **585**, 357
 Hinkle, J. 2021, TNSCR, **2021-2941**
 Hiramatsu, D., Howell, D. A., Moriya, T. J., et al. 2021, *ApJ*, **913**, 55
 Hunter, J. D. 2007, *CSE*, **9**, 90
 Jermyn, A. S., Bauer, E. B., Schwab, J., et al. 2023, *ApJS*, **265**, 15
 Jones, D. O., French, K. D., Agnello, A., et al. 2021, TNSTR, **2021-2917**
 Kasen, D., & Woosley, S. E. 2009, *ApJ*, **703**, 2205
 Kluyver, T., Ragan-Kelley, B., Pérez, F., et al. 2016, in Positioning and Power in Academic Publishing: Players, Agents and Agendas, ed. F. Loizides & B. Schmidt (Netherlands: IOS Press), 87
 Kumar, H., Bhalerao, V., Anupama, G. C., et al. 2022, *AJ*, **164**, 90
 Laplace, E., Justham, S., Renzo, M., et al. 2021, *A&A*, **656**, A58
 Lisakov, S. M., Dessart, L., Hillier, D. J., Waldman, R., & Livne, E. 2018, *MNRAS*, **473**, 3863
 Martínez, L., & Bersten, M. C. 2019, *A&A*, **629**, A124
 McKinney, W. 2010, Proc. of the 9th Python in Science Conf., ed. S. van der Walt & J. Millman, (SciPy), 56
 Moriya, T. J., Müller, B., Chan, C., Heger, A., & Blinnikov, S. I. 2019, *ApJ*, **880**, 21
 Moriya, T. J., Subrayan, B. M., Milisavljevic, D., & Blinnikov, S. I. 2023, *PASJ*, **75**, 634
 Morozova, V., Piro, A. L., Renzo, M., et al. 2015, *ApJ*, **814**, 63
 Murai, Y., Tanaka, M., Kawabata, M., et al. 2024, *MNRAS*, **528**, 4209
 Nagy, A. P., Ordasi, A., Vinkó, J., & Wheeler, J. C. 2014, *A&A*, **571**, A77
 Nagy, A. P., & Vinkó, J. 2016, *A&A*, **589**, A53
 Nakaoka, T., Kawabata, K. S., Maeda, K., et al. 2018, *ApJ*, **859**, 78
 Nicholl, M. 2018, *RNAAS*, **2**, 230
 pandas development team 2020, pandas-dev/pandas: Pandas, latest, Zenodo, doi:10.5281/zenodo.3509134
 Parrent, J., Branch, D., & Jeffery, D. 2010, SYNOW: A Highly Parameterized Spectrum Synthesis Code for Direct Analysis of SN Spectra, Astrophysics Source Code Library, ascl:1010.055
 Pastorello, A., Sauer, D., Taubenberger, S., et al. 2006, *MNRAS*, **370**, 1752
 Pastorello, A., Valenti, S., Zampieri, L., et al. 2009, *MNRAS*, **394**, 2266
 Paxton, B., Bildsten, L., Dotter, A., et al. 2011, *ApJS*, **192**, 3
 Paxton, B., Cantiello, M., Arras, P., et al. 2013, *ApJS*, **208**, 4
 Paxton, B., Marchant, P., Schwab, J., et al. 2015, *ApJS*, **220**, 15
 Paxton, B., Schwab, J., Bauer, E. B., et al. 2018, *ApJS*, **234**, 34
 Paxton, B., Smolec, R., Schwab, J., et al. 2019, *ApJS*, **243**, 10
 Perna, R., Duffell, P., Cantiello, M., & MacFadyen, A. I. 2014, *ApJ*, **781**, 119
 Pessi, P. J., Folatelli, G., Anderson, J. P., et al. 2019, *MNRAS*, **488**, 4239
 Popov, D. V. 1993, *ApJ*, **414**, 712
 Prabhu, T. P. 2014, *PINSA*, **80**, 887
 Pumo, M. L., Zampieri, L., Spiro, S., et al. 2017, *MNRAS*, **464**, 3013
 Reguitti, A., Pumo, M. L., Mazzali, P. A., et al. 2021, *MNRAS*, **501**, 1059
 Riess, A. G., Yuan, W., Macri, L. M., et al. 2022, *ApJL*, **934**, L7

- Sahu, D. K., Anupama, G. C., & Chakradhari, N. K. 2013, *MNRAS*, **433**, 2
- Schlafly, E. F., & Finkbeiner, D. P. 2011, *ApJ*, **737**, 103
- Schneider, S. E., Thuan, T. X., Mangum, J. G., & Miller, J. 1992, *ApJS*, **81**, 5
- Shingles, L., Smith, K. W., Young, D. R., et al. 2021, *TNSAN*, **7**, 1
- Singh, A., Teja, R. S., Moriya, T. J., et al. 2024, arXiv:2405.20989
- Smartt, S. J., Eldridge, J. J., Crockett, R. M., & Maund, J. R. 2009, *MNRAS*, **395**, 1409
- Smith, K. W., Smartt, S. J., Young, D. R., et al. 2020, *PASP*, **132**, 085002
- Smithsonian Astrophysical Observatory 2000, SAOImage DS9: A utility for displaying astronomical images in the X11 window environment, Astrophysics Source Code Library, ascl:0003.002
- Sollerman, J., Yang, S., Schulze, S., et al. 2021, *A&A*, **655**, A105
- Spiro, S., Pastorello, A., Pumo, M. L., et al. 2014, *MNRAS*, **439**, 2873
- Sukhbold, T., Ertl, T., Woosley, S. E., Brown, J. M., & Janka, H. T. 2016, *ApJ*, **821**, 38
- Szalai, T., Vinkó, J., Könyves-Tóth, R., et al. 2019, *ApJ*, **876**, 19
- Takáts, K., & Vinkó, J. 2012, *MNRAS*, **419**, 2783
- Teja, R. S., Singh, A., Sahu, D. K., et al. 2022, *ApJ*, **930**, 34
- Teja, R. S., Singh, A., Sahu, D. K., et al. 2023a, *ApJ*, **954**, 155
- Teja, R. S., Singh, A., Basu, J., et al. 2023b, *ApJL*, **954**, L12
- Thomas, R. C., Nugent, P. E., & Meza, J. C. 2011, *PASP*, **123**, 237
- Tody, D. 1993, in ASP Conf. Ser. 52, *Astronomical Data Analysis Software and Systems II*, ed. R. J. Hanisch, R. J. V. Brissenden, & J. Barnes (San Francisco, CA: ASP), 173
- Tonry, J. L., Denneau, L., Heinze, A. N., et al. 2018, *PASP*, **130**, 064505
- Tsvetkov, D. Y., Volnova, A. A., Shulga, A. P., et al. 2006, *A&A*, **460**, 769
- Utrobin, V. P., & Chugai, N. N. 2024, *MNRAS*, **527**, 6227
- Valenti, S., Howell, D. A., Stritzinger, M. D., et al. 2016, *MNRAS*, **459**, 3939
- Valerin, G., Pumo, M. L., Pastorello, A., et al. 2022, *MNRAS*, **513**, 4983
- Virtanen, P., Gommers, R., Oliphant, T. E., et al. 2020, *NatMe*, **17**, 261
- Young, D. R. 2020, *plot_atlas_fp.py*, v1.0.1, Zenodo, doi:10.5281/zenodo.10978968
- Yuan, F., Jerkstrand, A., Valenti, S., et al. 2016, *MNRAS*, **461**, 2003
- Zampieri, L., Pastorello, A., Turatto, M., et al. 2003, *MNRAS*, **338**, 711